COUPLED DICTIONARY LEARNING FOR MULTI-CONTRAST MRI RECONSTRUCTION

Pingfan Song[★]   *Lior Weizman*[♯]   *João F. C. Mota*[†]   *Yonina C. Eldar*[♯]   *Miguel R. D. Rodrigues*[★]

[★] Department of Electronic and Electrical Engineering, University College London, UK
[♯] Department of Electrical Engineering, Technion – Israel Institute of Technology, Israel
[†] School of Engineering and Physical Sciences, Heriot-Watt University, UK

ABSTRACT

Medical imaging tasks often involve multiple contrasts, such as T1- and T2-weighted magnetic resonance imaging (MRI) data. These contrasts capture information associated with the same underlying anatomy and thus exhibit similarities. In this paper, we propose a Coupled Dictionary Learning based multi-contrast MRI reconstruction (CDLMRI) approach to leverage an available guidance contrast to restore the target contrast. Our approach consists of three stages: coupled dictionary learning, coupled sparse denoising, and k-space consistency enforcing. The first stage learns a group of dictionaries that capture correlations among multiple contrasts. By capitalizing on the learned adaptive dictionaries, the second stage performs joint sparse coding to denoise the corrupted target image with the aid of a guidance contrast. The third stage enforces consistency between the denoised image and the measurements in the k-space domain. Numerical experiments on the retrospective under-sampling of clinical MR images demonstrate that incorporating additional guidance contrast via our design improves MRI reconstruction, compared to state-of-the-art approaches.

Index Terms— multi-contrast MRI, coupled dictionary learning, coupled sparse denoising, guidance information

1. INTRODUCTION

Magnetic Resonance Imaging (MRI) is a noninvasive and non-ionizing medical imaging technique that has been widely used for medical diagnosis, clinical analysis, and staging of disease. Owing to its versatility, different MRI pulse sequences produce images with different contrasts, such as Fluid-attenuated inversion recovery (FLAIR), T1-weighted, and T2-weighted. Each contrast images different physical properties of the tissues examined [1, 2]. The acquisition time of conventional brain multi-contrast MRI is at least 30 minutes, which can lead to discomfort in some patients and requires sedation for pediatric patients. Different image constrasts, however, are highly correlated, because they image the same underlying anatomy [3]. Such correlation can potentially be used to shorten acquisition time by partial acquisition of the target contrast, followed by reconstruction that takes into account other fully-sampled contrasts as guidance/reference.

MRI reconstruction from under-sampled measurements has been thoroughly investigated in the case of single contrast acquisition. The pioneering framework proposed by Lustig et al. [4],

motivated by compressive sensing theory [5–8], uses the fact that MR images are sampled in the spatial frequency domain (a.k.a. k-space) and can be represented as a sparse combination of fixed, predefined bases, for example, wavelets. Building on this work, Ravishankar et al. [9] proposed a dictionary learning based MRI reconstruction approach, DLMRI, which is based on the fact that patches of MR images can be sparsely represented with respect to a set of adaptive learned bases [10, 11]. Those adaptive bases contribute to improved performance of DLMRI over SparseMRI [4]. Both SparseMRI and DLMRI consider a single contrast.

The reconstruction of an MRI target contrast based on the availability of other contrasts has also been recently investigated in some works [3, 12–18]. For example, for the case where one contrast (the "target contrast") is under-sampled and the other is fully sampled and serves as guidance/reference, Weizman et al. [12, 13] proposed reference-based MRI, that exploits gray level similarity between T2-weighted and FLAIR, to reconstruct the target contrast (FLAIR) given the guidance contrast (T2-weighted). Their approach is specific to contrasts with gray level similarity, not to structural similarity which is our focus here. Ehrhardt et al. [3, 14] propose an approach, STVMRI, that exploits structure-guided total variation to integrate the location and direction priors from a guidance contrast into the reconstruction of the target contrast.

Inspired by DLMRI [9], we propose a coupled dictionary learning approach for multi-contrast MRI reconstruction, referred to as CDLMRI, for contrasts that exhibit structural similarity (e.g. T1-weighted and T2-weighted), a scenario more general than the one addressed in [12]. Specifically, our approach cycles between three stages: coupled dictionary learning, coupled sparse denoising and k-space consistency enforcing. The first stage learns a group of dictionaries that capture inherent structural similarity on textures, edges, boundaries, or other salient features across multiple contrasts. The second stage performs joint sparse coding using the learned adaptive dictionaries to denoise the corrupted target image with the aid of a guidance contrast. The third stage enforces consistency between the denoised image and the measurements in the k-space domain. Our approach shows significant advantages over the competing methods, DLMRI [9] and STVMRI [3] both in visual quality, and in peak signal-to-noise ratio (PSNR).

2. PROBLEM FORMULATION

We denote by $\mathbf{x}^{(1)} \in \mathcal{C}^N$ the vectorized 2D MR imaging contrast of size $\sqrt{N} \times \sqrt{N}$ to be reconstructed. The vector $\mathbf{y}^{(1)} \in \mathcal{C}^m$ denotes the under-sampled k-space measurements related to $\mathbf{x}^{(1)}$, and the matrix $\mathbf{F}_{u1} \in \mathcal{C}^{m \times N}$ denotes the corresponding under-sampled Fourier transform matrix. In addition, we assume that a fully-sampled guidance MR imaging contrast $\mathbf{x}^{(2)} \in \mathcal{C}^N$ is available. Our goal is to reconstruct $\mathbf{x}^{(1)}$ from its k-space samples $\mathbf{y}^{(1)}$ under the aid of the guidance image $\mathbf{x}^{(2)}$.

2.1. Data Model for Multi-contrast MRI Data

As we would like to utilize the structural similarity between $\mathbf{x}^{(1)}$ and $\mathbf{x}^{(2)}$, we first propose a data model that captures this similarity. Our data model works with image patches, instead of the entire image level, because a patch-based model is able to capture local image features effectively, as shown in other applications such as image denoising, super-resolution, inpainting, deblurring and demosaicing [19–25].

Let $\mathbf{x}_{ij}^{(1)} \in \mathcal{C}^n$ and $\mathbf{x}_{ij}^{(2)} \in \mathcal{C}^n$ denote the vector representations of image patch pairs of size $\sqrt{n} \times \sqrt{n}$ extracted from the image $\mathbf{x}^{(1)}$ and $\mathbf{x}^{(2)}$, respectively, where the tuple (i, j) denotes the coordinates of the top-left corner of the patches within the images. Formally, we write $\mathbf{x}_{ij}^{(1)} = \mathbf{R}_{ij}\mathbf{x}^{(1)}$ (resp. $\mathbf{x}_{ij}^{(2)} = \mathbf{R}_{ij}\mathbf{x}^{(2)}$), where the matrix $\mathbf{R}_{ij} \in \mathcal{C}^{n \times N}$ represents the operator that extracts patch $\mathbf{x}_{ij}^{(1)}$ (resp. $\mathbf{x}_{ij}^{(2)}$) from $\mathbf{x}^{(1)}$ (resp. $\mathbf{x}^{(2)}$). In order to capture both the similarity and discrepancy between two different contrasts, we assume that each patch pair $(\mathbf{x}_{ij}^{(1)}, \mathbf{x}_{ij}^{(2)})$ can be represented by a sum of two sparse representations: a common sparse component that is shared by both contrasts, and a unique sparse component for each contrast. In particular, we express the patch pair as follows:

$$\mathbf{x}_{ij}^{(1)} = \mathbf{\Psi}_c \mathbf{z}_{ij} + \mathbf{\Psi} \mathbf{u}_{ij}, \tag{1}$$

$$\mathbf{x}_{ij}^{(2)} = \mathbf{\Phi}_c \mathbf{z}_{ij} + \mathbf{\Phi} \mathbf{v}_{ij}, \tag{2}$$

where $\mathbf{z}_{ij} \in \mathbb{R}^K$ is the common sparse representation shared by both contrasts, $\mathbf{u}_{ij} \in \mathbb{R}^K$ is a sparse representation specific to contrast $\mathbf{x}^{(1)}$, and $\mathbf{v}_{ij} \in \mathbb{R}^K$ is a sparse representation specific to contrast $\mathbf{x}^{(2)}$; in addition, $\mathbf{\Psi}_c = [\boldsymbol{\psi}_{c1}, \cdots, \boldsymbol{\psi}_{cK}] \in \mathbb{R}^{n \times K}$ and $\mathbf{\Phi}_c = [\boldsymbol{\phi}_{c1}, \cdots, \boldsymbol{\phi}_{cK}] \in \mathbb{R}^{n \times K}$ are a pair of dictionaries associated with the common sparse representation $\mathbf{z}_{ij}$, whereas $\mathbf{\Psi} = [\boldsymbol{\psi}_1, \cdots, \boldsymbol{\psi}_K] \in \mathbb{R}^{n \times K}$ and $\mathbf{\Phi} = [\boldsymbol{\phi}_1, \cdots, \boldsymbol{\phi}_K] \in \mathbb{R}^{n \times K}$ are dictionaries associated with the sparse representations $\mathbf{u}_{ij}$ and $\mathbf{v}_{ij}$, respectively. Note that, this model can be generalized for $\mathbf{\Psi}$ and $\mathbf{\Phi}$ to have different number of atoms.

2.2. CDLMRI

Our goal is to leverage the proposed data model (1)-(2) in order to recover the target MRI contrast $\mathbf{x}^{(1)}$ given the guidance MRI contrast $\mathbf{x}^{(2)}$ and the k-space measurements $\mathbf{y}^{(1)}$. To this end, we propose Coupled Dictionary Learning for multi-contrast MRI reconstruction algorithm that attempts to solve the following optimization problem

$$\begin{aligned}
\underset{\substack{\mathbf{x}^{(1)}, \mathbf{z}_{ij}, \mathbf{u}_{ij}, \mathbf{v}_{ij} \\ \mathbf{\Phi}_c, \mathbf{\Phi}, \mathbf{\Psi}_c, \mathbf{\Psi}}}{\text{minimize}} \quad & \sum_{ij} \Big\{ \|\mathbf{R}_{ij}\mathbf{x}^{(1)} - (\mathbf{\Psi}_c \mathbf{z}_{ij} + \mathbf{\Psi}\mathbf{u}_{ij})\|_2^2 \\
& + \|\mathbf{R}_{ij}\mathbf{x}^{(2)} - (\mathbf{\Phi}_c \mathbf{z}_{ij} + \mathbf{\Phi}\mathbf{v}_{ij})\|_2^2 \\
& + \nu_1 \|\mathbf{F}_{u1}\mathbf{x}^{(1)} - \mathbf{y}^{(1)}\|_2^2 \Big\} \\
\text{subject to} \quad & \|\mathbf{z}_{ij}\|_0 \leq s_c, \|\mathbf{u}_{ij}\|_0 \leq s_1, \|\mathbf{v}_{ij}\|_0 \leq s_2, \forall i, j, \\
& \left\| \begin{bmatrix} \boldsymbol{\psi}_{ck} \\ \boldsymbol{\phi}_{ck} \end{bmatrix} \right\|_2^2 \leq 1, \|\boldsymbol{\psi}_k\|_2^2 \leq 1, \|\boldsymbol{\phi}_k\|_2^2 \leq 1, \forall k.
\end{aligned} \tag{3}$$

Note that the first two terms in the objective ensure that the image patches are consistent with their postulated model and the third term in the objective ensures that the target image is consistent with its k-space measurements; the parameter $\nu_1 \geq 0$ balances between model and measurements fidelity. Moreover, the first set of constraints induce sparsity for the vectors $\mathbf{z}_{ij}, \mathbf{u}_{ij}, \mathbf{v}_{ij}$ and the second set of constraints normalizes the atoms of the dictionaries in order to remove the scaling ambiguity and avoid trivial solutions.

Problem (3) is highly nonconvex. Therefore, we attempt to solve this problem by alternating between three stages over a number of

---

Algorithm 1 CDLMRI Algorithm

Input: Under-sampled k-space measurements: $\mathbf{y}^{(1)}$; Guidance contrast: $\mathbf{x}^{(2)}$; Parameter: ν_1; Sparse constraints: s_c, s_1, s_2; Number of iterations for CDL: L; Number of cycles for CDLMRI: T; Number of overlapping patches at each pixel: β.

Output: Estimated $\tilde{\mathbf{x}}^{(1)}$.

Initialization: Initialize $\mathbf{x}^{(1)}$ as $\mathbf{x}^{(1)} = \mathbf{F}_{u1}^H \mathbf{y}^{(1)}$.

Optimization:

1: **for** $t = 1, \cdots, T$ **do**
2:   **Coupled Dictionary Learning stage.** Estimate the coupled dictionaries $\mathbf{\Psi}_c, \mathbf{\Psi}, \mathbf{\Phi}_c, \mathbf{\Phi}$ using Algorithm 2.
3:   **Coupled Sparse Denoising stage.** Estimate the sparse representations $\mathbf{z}_{ij}$ and $\mathbf{u}_{ij}$ by solving (4) and (5) using the OMP algorithm. It also involves estimating the denoised patches $\hat{\mathbf{x}}_{ij}^{(1)} = \mathbf{\Psi}_c \mathbf{z}_{ij} + \mathbf{\Psi}\mathbf{u}_{ij}$ from $\mathbf{z}_{ij}, \mathbf{u}_{ij}$.
4:   k-**space Consistency Enforcing stage.** Estimate the target contrast $\tilde{\mathbf{x}}^{(1)}$ from estimated k-space samples $\tilde{\mathbf{y}}^{(1)}$ via (13) and (8).
5: **end for**

---

cycles: 1) Coupled dictionary learning, 2) Coupled sparse denoising, and 3) k-space consistency enforcing, as shown in Algorithm 1.

Stage 1) Coupled Dictionary Learning. In the first cycle, $\mathbf{x}^{(1)}$ is initialized as $\mathbf{F}_{u1}^H \mathbf{y}^{(1)}$ (i.e. $\mathbf{x}^{(1)}$ is set to be equal to the inverse DFT of the zero-filled Fourier measurements). In the remaining cycles, in this stage, $\mathbf{x}^{(1)}$ will be the output of Stage 3) from the previous cycle. In particular, for fixed $\mathbf{x}^{(1)}$, we attempt to solve (3) via alternating minimization where in a first step we update $\mathbf{z}_{ij}, \mathbf{u}_{ij}, \mathbf{v}_{ij}$ for fixed $\mathbf{\Psi}_c, \mathbf{\Psi}, \mathbf{\Phi}_c, \mathbf{\Phi}$ and in a second step we update $\mathbf{\Psi}_c, \mathbf{\Psi}, \mathbf{\Phi}_c, \mathbf{\Phi}$ for fixed $\mathbf{z}_{ij}, \mathbf{u}_{ij}, \mathbf{v}_{ij}$. As shown in Algorithm 2, the sparse coding step is addressed using the orthogonal matching pursuit (OMP) algorithm [21, 26] and dictionary update step is adapted from the Block Coordinate Descent [27]. Note that, since a single image consists of large amount of patches, we only use a subset of the patches to constitute the training dataset $\mathbf{X}^{(1)} = [\cdots, \mathbf{x}_{ij}^{(1)}, \cdots]$ and $\mathbf{X}^{(2)} = [\cdots, \mathbf{x}_{ij}^{(2)}, \cdots]$ in Stage 1) to save training time.

Stage 2) Coupled Sparse Denoising. As the sparse representations computed in Stage 1) are associated only with a subset of the collection of image patches, it is necessary to perform one additional sparse denoising stage. In addition, we also introduce linearly decreasing error thresholds to fine tune the sparse representations, since this operation has been shown experimentally to improve the dealiasing and denoising performance. In particular, we give priority to perform the following optimization in order to determine an approximation to the common sparse representations associated with the various image patches:

$$\begin{aligned}
\min_{\mathbf{z}_{ij}} \max\{ &\|\mathbf{R}_{ij}\mathbf{x}^{(1)} - \mathbf{\Psi}_c \mathbf{z}_{ij}\|_2^2 + \|\mathbf{R}_{ij}\mathbf{x}^{(2)} - \mathbf{\Phi}_c \mathbf{z}_{ij}\|_2^2 - \epsilon_c, 0\} \\
\text{s.t.} \quad & \|\mathbf{z}_{ij}\|_0 \leq s_c.
\end{aligned} \tag{4}$$

We then perform the following optimization in order to determine an approximation to the unique sparse representations associated with the various target image patches:

$$\begin{aligned}
\min_{\mathbf{u}_{ij}} \quad \max\{ &\|\mathbf{R}_{ij}\mathbf{x}^{(1)} - \mathbf{\Psi}_c \mathbf{z}_{ij} - \mathbf{\Psi}\mathbf{u}_{ij}\|_2^2 - \epsilon_1, 0\} \\
\text{s.t.} \quad & \|\mathbf{u}_{ij}\|_0 \leq s_1.
\end{aligned} \tag{5}$$

Here ϵ_c and ϵ_1 denote the expected error thresholds which are used, together with s_c and s_1, in OMP as the stopping criteria. The above

Algorithm 2 Coupled Dictionary Learning algorithm

Input: A subset of estimated target image patches: $\mathbf{X}^{(1)} = [\cdots, \mathbf{x}_{ij}^{(1)}, \cdots]$; The subset of the corresponding guidance image patches: $\mathbf{X}^{(2)} = [\cdots, \mathbf{x}_{ij}^{(2)}, \cdots]$; Sparse constraints: s_c, s_1, s_2; Number of iterations: L;

Output: Coupled dictionaries: $\boldsymbol{\Psi}_c, \boldsymbol{\Phi}_c, \boldsymbol{\Psi}, \boldsymbol{\Phi}$.

Initialization: Initialize each dictionary with randomly selected patches of the corresponding contrast. Initialize all sparse representations with zeros.

Optimization:

1: **for** $l = 1, \cdots, L$ **do**
2:    **a) Sparse Coding step.** This step updates the sparse codes for fixed dictionaries. Note that steps 3 - 6 apply the OMP algorithm [26] to estimate $\mathbf{Z} = [\cdots, \mathbf{z}_{ij}, \cdots]$ given data $\mathbf{X}^{(1)}$, $\mathbf{X}^{(2)}$ and dictionaries $\boldsymbol{\Psi}_c, \boldsymbol{\Phi}_c$.
3:    Initialize the active set $\Gamma = \emptyset$ and $\mathbf{z}_{ij} \leftarrow 0$.
4:    **while** $|\Gamma| < s_c$ **do**
5:       select a new coordinate $\hat{k}$ that leads to the smallest residual and, then update the active set and the solution $\mathbf{z}_{ij}$:

$$(\hat{k}, \hat{\boldsymbol{\alpha}}) \in \underset{k \in \Gamma^c, \boldsymbol{\alpha} \in \mathbb{R}^{|\Gamma|+1}}{\arg\min} \left\| \begin{bmatrix} \mathbf{x}_{ij}^{(1)} \\ \mathbf{x}_{ij}^{(2)} \end{bmatrix} - \begin{bmatrix} \boldsymbol{\Psi}_c \\ \boldsymbol{\Phi}_c \end{bmatrix}_{\Gamma \cup \{k\}} \boldsymbol{\alpha} \right\|_2^2 ;$$

$$\Gamma \leftarrow \Gamma \cup \{\hat{k}\}; \quad \mathbf{z}_{ij_\Gamma} \leftarrow \hat{\boldsymbol{\alpha}}; \quad \mathbf{z}_{ij_{\Gamma^c}} \leftarrow 0;$$

6:    **end while**
7:    This OMP process is repeated to estimate $\mathbf{U} = [\cdots, \mathbf{u}_{ij}, \cdots]$ and $\mathbf{V} = [\cdots, \mathbf{v}_{ij}, \cdots]$ given $\mathbf{X}^{(1)} - \boldsymbol{\Psi}_c \mathbf{Z} = \boldsymbol{\Psi}\mathbf{U}$ and $\mathbf{X}^{(2)} - \boldsymbol{\Phi}_c \mathbf{Z} = \boldsymbol{\Phi}\mathbf{V}$, with sparsity constraints s_1 and s_2, respectively.

8:    **b) Dictionary Update step.** This step updates the dictionaries for fixed sparse codes.
9:    **for** $k = 1, \cdots, K$ **do**
10:      Update the k-th column of $\boldsymbol{\Psi}_c$ and $\boldsymbol{\Phi}_c$ as follows:

$$\mathbf{d}_k \leftarrow \frac{1}{\mathbf{z}^k \mathbf{z}^{k^T}} \left(\begin{bmatrix} \mathbf{X}^{(1)} - \boldsymbol{\Psi}\mathbf{U} \\ \mathbf{X}^{(2)} - \boldsymbol{\Phi}\mathbf{V} \end{bmatrix} - \begin{bmatrix} \boldsymbol{\Psi}_c \\ \boldsymbol{\Phi}_c \end{bmatrix} \mathbf{Z} \right) \mathbf{z}^{k^T} + \begin{bmatrix} \boldsymbol{\psi}_{ck} \\ \boldsymbol{\phi}_{ck} \end{bmatrix}$$

$$\begin{bmatrix} \boldsymbol{\psi}_{ck} \\ \boldsymbol{\phi}_{ck} \end{bmatrix} \leftarrow \frac{\mathbf{d}_k}{\max(\|\mathbf{d}_k\|_2, 1)}$$

     where $\mathbf{z}^k$ denotes the k-th row of $\mathbf{Z}$.

11:    **end for**
12:    **for** $k = 1, \cdots, K$ **do**
13:      Update the k-th column of $\boldsymbol{\Psi}$ and $\boldsymbol{\Phi}$ as follows:

$$\boldsymbol{\psi}_k \leftarrow \frac{1}{\mathbf{u}^k \mathbf{u}^{k^T}}(\mathbf{X}^{(1)} - \boldsymbol{\Psi}_c \mathbf{Z} - \boldsymbol{\Psi}\mathbf{U})\mathbf{u}^{k^T} + \boldsymbol{\psi}_k$$

$$\boldsymbol{\phi}_k \leftarrow \frac{1}{\mathbf{v}^k \mathbf{v}^{k^T}}(\mathbf{X}^{(2)} - \boldsymbol{\Phi}_c \mathbf{Z} - \boldsymbol{\Phi}\mathbf{V})\mathbf{v}^{k^T} + \boldsymbol{\phi}_k$$

$$\boldsymbol{\phi}_k \leftarrow \frac{\boldsymbol{\phi}_k}{\max(\|\boldsymbol{\phi}_k\|_2, 1)} ; \boldsymbol{\psi}_k \leftarrow \frac{\boldsymbol{\psi}_k}{\max(\|\boldsymbol{\psi}_k\|_2, 1)}$$

     where $\mathbf{u}^k$ (resp. $\mathbf{v}^k$) denotes the k-th row of $\mathbf{U}$ (resp. $\mathbf{V}$).

14:    **end for**
15: **end for**

---

formulations imply that once the objective value for (i, j)-th patch decreases below the expected error threshold, there is no need to find a better point and so we terminate the OMP loop. Otherwise, the OMP program keeps iterating until s_c (resp. s_1) non-zero values are retrieved for $\mathbf{z}_{ij}$ (resp. $\mathbf{u}_{ij}$). In addition, as the quality of the target image improves along the entire cycles, we decrease the thresholds ϵ_c and ϵ_1 linearly at each cycle. This strategy significantly accelerates the convergence speed, as well as allows us to dynamically control the real sparsity of each patch more effectively.

Given the sparse representations $\mathbf{z}_{ij}$ and $\mathbf{u}_{ij}$, we obtain each denoised patch as $\hat{\mathbf{x}}_{ij}^{(1)} = \boldsymbol{\Psi}_c \mathbf{z}_{ij} + \boldsymbol{\Psi}\mathbf{u}_{ij}$, where $\boldsymbol{\Psi}_c$ and $\boldsymbol{\Psi}$ are learned dictionaries in the Stage 1).

Stage 3) k-space Consistency Enforcing. Finally, in this stage, we enforce the consistency between the denoised image and its measurements in the k-space domain, similar to DLMRI [9]. In particular, given the estimated patches $\hat{\mathbf{x}}_{ij}^{(1)}$ from Stage 2), this step is formulated as a least squares problem:

$$\min_{\mathbf{x}^{(1)}} \sum_{ij} \left\| \mathbf{R}_{ij}\mathbf{x}^{(1)} - \hat{\mathbf{x}}_{ij}^{(1)} \right\|_2^2 + \nu_1 \left\| \mathbf{F}_{u1}\mathbf{x}^{(1)} - \mathbf{y}^{(1)} \right\|_2^2 , \quad (6)$$

By assuming that patches wrap around at image boundaries (which implies that the number of overlapping patches occurring at each pixel is equal), we immediately obtain the solution:

$$\tilde{\mathbf{x}}^{(1)} = \mathbf{F}^H \tilde{\mathbf{y}}^{(1)} \quad (7)$$

where $\mathbf{F}^H$ denotes the conjugate of the Fourier transform matrix; $\tilde{\mathbf{y}}^{(1)}$ denotes the estimated k-space samples and can be expressed as follows:

$$\tilde{\mathbf{y}}_{pq}^{(1)} = \begin{cases} \left(\mathbf{F}\hat{\mathbf{x}}^{(1)} \right)_{pq}, & (p, q) \notin \Omega^{(1)} \\ \frac{1}{1 + \tilde{\nu}_1} \left(\mathbf{F}\hat{\mathbf{x}}^{(1)} + \tilde{\nu}_1 \mathbf{F}\mathbf{F}_{u1}^H \mathbf{y}^{(1)} \right)_{pq}, & (p, q) \in \Omega^{(1)} \end{cases} \quad (8)$$

where $\tilde{\nu}_1 = \nu_1/\beta$, $\hat{\mathbf{x}}^{(1)} = \frac{1}{\beta}\sum_{ij} \mathbf{R}_{ij}^H \hat{\mathbf{x}}_{ij}^{(1)}$ represents the denoised image, and β denotes the number of overlapping patches at the corresponding pixel location in $\mathbf{x}^{(1)}$. We denote by $\Omega^{(1)}$ the subset of k-space that has been sampled and by $\tilde{\mathbf{y}}_{pq}^{(1)}$ the updated value at location (p, q) in the k-space.

The overall process consisting of the three stages is repeated over a number of cycles, which has been summarized in Algorithm 1.

3. EXPERIMENTS

In this section, we conduct some practical experiments to evaluate the performance of the proposed algorithm. Similar to previous approaches [3, 9, 12, 28–30], the data acquisition was simulated by retrospectively under-sampling the 2D discrete Fourier transform of clinical magnitude MR images. The sampling masks include Cartesian 1D and 2D random sampling. We compare the proposed approach with DLMRI [9] to show the benefits of integrating guidance information into the MRI reconstruction task. DLMRI [9] is also based on dictionary learning techniques, but it does not use a guidance contrast to aid the reconstruction of the target contrast. We also compare with SVTMRI [3] which is also based on the use of a guidance contrast to aid the reconstruction of the target one.

In the experiments, we set $\sqrt{N} \times \sqrt{N} = 256 \times 256$, $\sqrt{n} \times \sqrt{n} =$
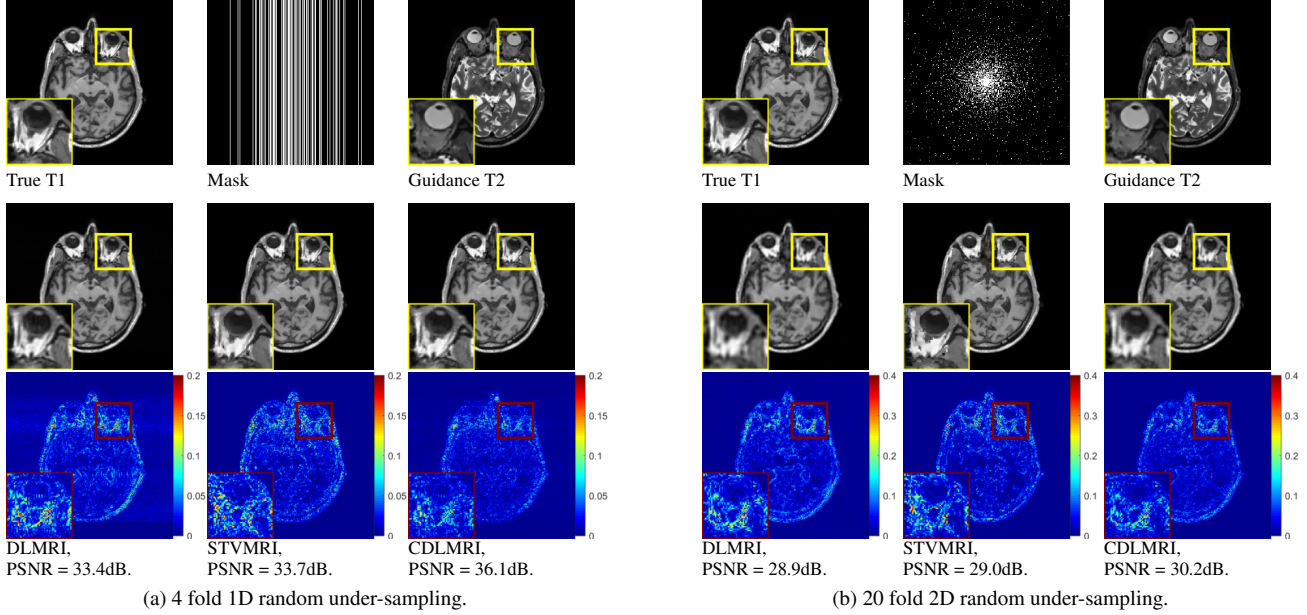
True T1 | **Mask** | **Guidance T2**

DLMRI, PSNR = 33.4dB. | STVMRI, PSNR = 33.7dB. | CDLMRI, PSNR = 36.1dB.

(a) 4 fold 1D random under-sampling.

DLMRI, PSNR = 28.9dB. | STVMRI, PSNR = 29.0dB. | CDLMRI, PSNR = 30.2dB.

(b) 20 fold 2D random under-sampling.

Fig. 1. Reconstruction from Cartesian under-sampling. In each sub-figure, the first row shows the groundtruth T1-weighted, sampling mask and guidance modality T2-weighted. The second and third rows show the reconstructed images and the corresponding residual error from DLMRI [9], STVMRI [3], and the proposed approaches. It can be seen that the proposed approach reliably reconstructs fine details and substantially suppresses aliasing, noise and artifacts, leading to the smallest residual error.

8×8, $K = 512$, $L = 50$, $T = 60$, $s_c = 6$, $s_1 = s_2 = 2$, $\epsilon_c = 0.1 \downarrow 0.005$ (meaning: ϵ_c is set to 0.1 in the beginning and linearly decreases to 0.005 along the cycles.), $\epsilon_1 = 0.09 \downarrow 0.004$, $\beta = 64$, $\nu_1 = \infty$ (for noise-free situation), and undersampling factor = 4 fold and 20 fold for the Cartesian 1D and 2D random sampling, respectively.

The visual performance is shown in Fig. 1. It can be seen that the reconstructed image and corresponding residual from DLMRI [9] introduce noticeable aliasing, noise and blurred areas. In comparison, the edges and outlines in the reconstructed image from STVMRI [3] are very sharp, thereby more visually appealing in some high-frequency areas. However, notice that some areas in the results of STVMRI [3] have been over-sharpened, thus introducing nonnegligible artifacts. In contrast, our approach substantially attenuates aliasing and noise and, at the same time, reliably restores fine details and suppresses artifacts, leading to a more comprehensive and interpretable reconstruction. The performance improvement is also demonstrated by the PSNR values.

Fig. 2 shows the learned coupled dictionaries from the T1- and T2- weighted MRI images. It can be seen that the atom pairs from common dictionaries Ψ_c, Φ_c capture associated edges, blobs and textures with the same direction and location. Most of them exhibit considerable resemblance to each other, but with opposite intensity. This phenomenon is consistent with MRI characteristics, such as Cerebrospinal fluid (CSF) being dark in T1-weighted contrast and bright in T2-weighted. This outcome indicates that the common dictionaries are able to capture the similarity between T1-weighted and T2-weighted contrasts. In comparison, the learned unique dictionaries Ψ, Φ represent the disparities of these modalities and therefore rarely exhibit similarity.

4. CONCLUSION

We presented an adaptive multi-contrast MRI reconstruction framework that capitalizes on both patch-based sparsity priors induced by
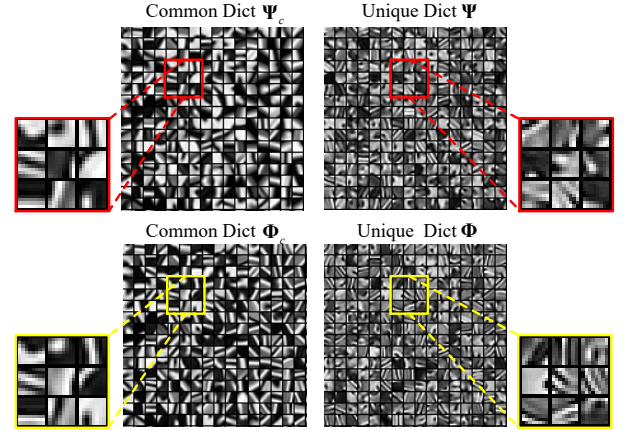

Fig. 2. Learned coupled dictionaries from T1 and T2-weighted contrasts; 256 atoms are shown. The top row displays the common and unique dictionaries for the T1-weighted contrast. The bottom row displays dictionaries learned from corresponding T2-weighted contrast. It can be seen that common dictionaries exhibit atoms with similar structure.

coupled dictionaries and structure similarity priors from the guidance contrast. The coupled dictionaries are trained directly on the target images and thus are adaptive to the contrast of interest. In addition, they also capture the correlations between T1- and T2-weighted contrasts, thereby beneficial information can be extracted from the guidance contrast to aid the reconstruction of the target contrast. Practical experiments demonstrate the superior performance of our design and significant advantage over competing methods. In the future, we will adapt our algorithm for other practical sampling patterns, such as radial sampling and also explore the impact of noise.

5. REFERENCES

[1] Z.-P. Liang and P. C. Lauterbur, *Principles of magnetic resonance imaging: a signal processing perspective.* SPIE Optical Engineering Press, 2000.

[2] D. W. McRobbie, E. A. Moore *et al.*, *MRI from Picture to Proton.* Cambridge university press, 2007.

[3] M. J. Ehrhardt and M. M. Betcke, "Multicontrast MRI reconstruction with structure-guided total variation," *SIAM Journal on Imaging Sciences*, vol. 9, no. 3, pp. 1084–1106, 2016.

[4] M. Lustig, D. Donoho *et al.*, "Sparse MRI: The application of compressed sensing to rapid MR imaging," *Magn. Reson. Med.*, vol. 58, pp. 1182–1195, 2007.

[5] D. Donoho, "Compressed sensing," *IEEE Trans. Info. Theory*, vol. 52, no. 4, pp. 1289–1306, 2006.

[6] E. Candès, J. Romberg *et al.*, "Robust uncertainty principles: Exact signal reconstruction from highly incomplete frequency information," *IEEE Trans. Info. Theory*, vol. 52, no. 2, pp. 489–509, 2006.

[7] Y. C. Eldar and G. Kutyniok, *Compressed sensing: theory and applications.* Cambridge University Press, 2012.

[8] Y. C. Eldar, *Sampling Theory: Beyond Bandlimited Systems.* Cambridge University Press, 2015.

[9] S. Ravishankar and Y. Bresler, "MR image reconstruction from highly undersampled k-space data by dictionary learning," *IEEE Trans. Med. Imag.*, vol. 30, no. 5, pp. 1028–1041, 2011.

[10] B. A. Olshausen *et al.*, "Emergence of simple-cell receptive field properties by learning a sparse code for natural images," *Nature*, vol. 381, no. 6583, pp. 607–609, 1996.

[11] M. Aharon, M. Elad *et al.*, "K-svd: An algorithm for designing overcomplete dictionaries for sparse representation," *IEEE Trans. Signal Process.*, vol. 54, no. 11, pp. 4311–4322, 2006.

[12] L. Weizman, Y. C. Eldar *et al.*, "Reference-based MRI," *Medical physics*, vol. 43, no. 10, pp. 5357–5369, 2016.

[13] L. Weizman, Y. C. Eldar *et al.*, "Compressed sensing for longitudinal MRI: An adaptive-weighted approach," *Medical physics*, vol. 42, no. 9, pp. 5195–5208, 2015.

[14] M. Ehrhardt, "Joint reconstruction for multi-modality imaging with common structure," Ph.D. dissertation, UCL (University College London), 2015.

[15] J. Huang, C. Chen *et al.*, "Fast multi-contrast mri reconstruction," *Magnetic resonance imaging*, vol. 32, no. 10, pp. 1344–1352, 2014.

[16] B. Bilgic, V. K. Goyal *et al.*, "Multi-contrast reconstruction with bayesian compressed sensing," *Magn. Reson. Med.*, vol. 66, no. 6, pp. 1601–1615, 2011.

[17] X. Qu, Y. Hou *et al.*, "Magnetic resonance image reconstruction from undersampled measurements using a patch-based nonlocal operator," *Medical image analysis*, vol. 18, no. 6, pp. 843–856, 2014.

[18] I. Chatnuntawech, A. Martin *et al.*, "Vectorial total generalized variation for accelerated multi-channel multi-contrast mri," *Magnetic resonance imaging*, vol. 34, no. 8, pp. 1161–1170, 2016.

[19] M. Elad and M. Aharon, "Image denoising via sparse and redundant representations over learned dictionaries," *IEEE Trans. Image Process.*, vol. 15, no. 12, pp. 3736–3745, 2006.

[20] P. Chatterjee and P. Milanfar, "Patch-based near-optimal image denoising," *IEEE Trans. Imag. Proc.*, vol. 21, no. 4, pp. 1635–1649, 2012.

[21] J. Mairal, F. Bach *et al.*, "Sparse modeling for image and vision processing," *Foundations and Trends® in Computer Graphics and Vision*, vol. 8, no. 2-3, pp. 85–283, 2014.

[22] J. Mairal, F. Bach *et al.*, "Non-local sparse models for image restoration," in *Proc. IEEE Int. Conf. Comput. Vision.* IEEE, 2009, pp. 2272–2279.

[23] R. Timofte, V. De Smet *et al.*, "Anchored neighborhood regression for fast example-based super-resolution," in *Proc. IEEE Int. Conf. Comput. Vision.* IEEE, 2013, pp. 1920–1927.

[24] R. Timofte, V. De Smet *et al.*, "A+: Adjusted anchored neighborhood regression for fast super-resolution," in *Proc. Asian Conf. Comput. Vision.* Springer, 2014, pp. 111–126.

[25] J. Yang, J. Wright *et al.*, "Image super-resolution via sparse representation," *IEEE Trans. Image Process.*, vol. 19, no. 11, pp. 2861–2873, 2010.

[26] J. A. Tropp and A. C. Gilbert, "Signal recovery from random measurements via orthogonal matching pursuit," *IEEE Trans. Inform. Theory*, vol. 53, no. 12, pp. 4655–4666, 2007.

[27] J. Mairal, F. Bach *et al.*, "Online learning for matrix factorization and sparse coding," *The Journal of Machine Learning Research*, vol. 11, pp. 19–60, 2010.

[28] S. Ma, W. Yin *et al.*, "An efficient algorithm for compressed mr imaging using total variation and wavelets," in *Computer Vision and Pattern Recognition, 2008. CVPR 2008. IEEE Conference on.* IEEE, 2008, pp. 1–8.

[29] J. Yang, Y. Zhang *et al.*, "A fast alternating direction method for tvl1-l2 signal reconstruction from partial fourier data," *IEEE Journal of Selected Topics in Signal Processing*, vol. 4, no. 2, pp. 288–297, 2010.

[30] J. Trzasko and A. Manduca, "Highly undersampled magnetic resonance image reconstruction via homotopic ℓ_0-minimization," *IEEE Trans. Med. Imag.*, vol. 28, no. 1, pp. 106–121, 2009.

Appendix A: CDLMRI

We provide more details in relation to Section 2.2 CDLMRI in this appendix.

Stage 1) Coupled Dictionary Learning (details). The dictionary update step is to solve the optimization problem:

$$\underset{\boldsymbol{\Psi}_c,\boldsymbol{\Psi},\boldsymbol{\Phi}_c,\boldsymbol{\Phi}}{\text{minimize}} \sum_{ij} \left\{ \|\mathbf{R}_{ij}\mathbf{x}^{(1)} - (\boldsymbol{\Psi}_c\mathbf{z}_{ij} + \boldsymbol{\Psi}\mathbf{u}_{ij})\|_2^2 \right.$$
$$\left. + \|\mathbf{R}_{ij}\mathbf{x}^{(2)} - (\boldsymbol{\Phi}_c\mathbf{z}_{ij} + \boldsymbol{\Phi}\mathbf{v}_{ij})\|_2^2 \right\} \quad (9)$$
$$\text{subject to } \left\| \begin{bmatrix} \boldsymbol{\psi}_{ck} \\ \boldsymbol{\phi}_{ck} \end{bmatrix} \right\|_2^2 \le 1, \|\boldsymbol{\psi}_k\|_2^2 \le 1, \|\boldsymbol{\phi}_k\|_2^2 \le 1, \forall k$$

Given a subset of the patches to constitute the training dataset $\mathbf{X}^{(1)} = [\cdots, \mathbf{x}_{ij}^{(1)}, \cdots]$ and $\mathbf{X}^{(2)} = [\cdots, \mathbf{x}_{ij}^{(2)}, \cdots]$ in Stage 1), the optimization problem (9) is equivalent to:

$$\underset{\boldsymbol{\Psi}_c,\boldsymbol{\Psi},\boldsymbol{\Phi}_c,\boldsymbol{\Phi}}{\text{minimize}} \left\| \begin{bmatrix} \mathbf{X}^{(1)} - \boldsymbol{\Psi}\mathbf{U} \\ \mathbf{X}^{(2)} - \boldsymbol{\Phi}\mathbf{V} \end{bmatrix} - \begin{bmatrix} \boldsymbol{\Psi}_c \\ \boldsymbol{\Phi}_c \end{bmatrix} \mathbf{Z} \right\|_F^2$$
$$\text{subject to } \left\| \begin{bmatrix} \boldsymbol{\psi}_{ck} \\ \boldsymbol{\phi}_{ck} \end{bmatrix} \right\|_2^2 \le 1, \|\boldsymbol{\psi}_k\|_2^2 \le 1, \|\boldsymbol{\phi}_k\|_2^2 \le 1, \forall k$$

where, $\mathbf{Z} = [\cdots, \mathbf{z}_{ij}^{(1)}, \cdots], \mathbf{U} = [\cdots, \mathbf{u}_{ij}^{(1)}, \cdots], \mathbf{V} = [\cdots, \mathbf{v}_{ij}^{(1)}, \cdots]$. Taking the dictionary update of $\boldsymbol{\Psi}_c$ and $\boldsymbol{\Phi}_c$ for example, we update the atom pairs one by one. For the k-th atom pair $\boldsymbol{\psi}_c$ and $\boldsymbol{\phi}_c$, we can immediately establish that

$$\mathbf{d}_k \leftarrow \min_{\mathbf{d}} \left\| \begin{bmatrix} \mathbf{X}^{(1)} - \boldsymbol{\Psi}\mathbf{U} \\ \mathbf{X}^{(2)} - \boldsymbol{\Phi}\mathbf{V} \end{bmatrix} - \begin{bmatrix} \boldsymbol{\Psi}_c \\ \boldsymbol{\Phi}_c \end{bmatrix} \mathbf{Z} + \begin{bmatrix} \boldsymbol{\psi}_{ck} \\ \boldsymbol{\phi}_{ck} \end{bmatrix} \mathbf{z}^k - \mathbf{d}\mathbf{z}^k \right\|_F^2$$
$$\text{s.t. } \|\mathbf{d}\|_2^2 \le 1,$$

By expanding the Frobenius norm and removing the constant term, it turns out that the above problem is equivalent to the optimization problem

$$\min_{\mathbf{d}} \frac{1}{2} \|\mathbf{d}\mathbf{z}^k\|_F^2 - \mathbf{d}^T \left(\begin{bmatrix} \mathbf{X}^{(1)} - \boldsymbol{\Psi}\mathbf{U} \\ \mathbf{X}^{(2)} - \boldsymbol{\Phi}\mathbf{V} \end{bmatrix} - \begin{bmatrix} \boldsymbol{\Psi}_c \\ \boldsymbol{\Phi}_c \end{bmatrix} \mathbf{Z} + \begin{bmatrix} \boldsymbol{\psi}_{ck} \\ \boldsymbol{\phi}_{ck} \end{bmatrix} \mathbf{z}^k \right) \mathbf{z}^{k^T}$$
$$\text{s.t. } \|\mathbf{d}\|_2^2 \le 1,$$

where $\mathbf{z}^k$ denotes the k-th row of $\mathbf{Z}$.[1] We compute the derivative of the objective w.r.t. $\mathbf{d}$, leading to a norm equation:

$$\mathbf{d}_k \leftarrow \frac{1}{\mathbf{z}^k\mathbf{z}^{k^T}} \left(\begin{bmatrix} \mathbf{X}^{(1)} - \boldsymbol{\Psi}\mathbf{U} \\ \mathbf{X}^{(2)} - \boldsymbol{\Phi}\mathbf{V} \end{bmatrix} - \begin{bmatrix} \boldsymbol{\Psi}_c \\ \boldsymbol{\Phi}_c \end{bmatrix} \mathbf{Z} \right) \mathbf{z}^{k^T} + \begin{bmatrix} \boldsymbol{\psi}_{ck} \\ \boldsymbol{\phi}_{ck} \end{bmatrix}$$

Then, we apply the ℓ_2 norm constraint.

$$\begin{bmatrix} \boldsymbol{\psi}_{ck} \\ \boldsymbol{\phi}_{ck} \end{bmatrix} = \mathbf{d}_k \leftarrow \frac{\mathbf{d}_k}{\max(\|\mathbf{d}_k\|_2, 1)}$$

The dictionary update of $\boldsymbol{\Psi}$ and $\boldsymbol{\Phi}$ is performed in a similar way. In order to accelerate the training, the proposed algorithm can be updated to online training version without difficulty.

Stage 3) k-space Consistency Enforcing (details). In this stage, we aim to enforce consistency between the denoised image and its measurements in the k-space domain. In particular, given the estimated patches $\hat{\mathbf{x}}_{ij}^{(1)}$ from Stage 2), this step is formulated as a least square problem:

$$\min_{\mathbf{x}^{(1)}} \sum_{ij} \left\| \mathbf{R}_{ij}\mathbf{x}^{(1)} - \hat{\mathbf{x}}_{ij}^{(1)} \right\|_2^2 + \nu_1 \left\| \mathbf{F}_{u1}\mathbf{x}^{(1)} - \mathbf{y}^{(1)} \right\|_2^2, \quad (10)$$

which admits an analytical solution satisfying the normal equation

$$\left(\sum_{ij} \mathbf{R}_{ij}^H\mathbf{R}_{ij} + \nu_1\mathbf{F}_{u1}^H\mathbf{F}_{u1} \right) \mathbf{x}^{(1)} = \sum_{ij} \mathbf{R}_{ij}^H\hat{\mathbf{x}}_{ij}^{(1)} + \nu_1\mathbf{F}_{u1}^H\mathbf{y}^{(1)},$$
$$(11)$$

where the superscript $()^H$ denotes the Hermitian transpose operation. The term $\sum_{ij}\mathbf{R}_{ij}^H\mathbf{R}_{ij} \in \mathcal{C}^{N\times N}$ is a diagonal matrix where each diagonal entry is the number of overlapping patches at the corresponding pixel location in $\mathbf{x}^{(1)}$. Assuming that patches wrap around at image boundaries, the number of overlapping patches at each pixel is the same, denoted by β.[2] Thus, the term $\frac{1}{\beta}\sum_{ij}\mathbf{R}_{ij}^H\hat{\mathbf{x}}_{ij}^{(1)}$ represents the denoised image $\hat{\mathbf{x}}^{(1)}$, where the intensity value of each pixel is the average of all the overlapping patches that cover this pixel. Multiplying by the normalized full Fourier transform matrix $\mathbf{F}$ on the both sides of equation (11) leads to

$$\left(\mathbf{F}\sum_{ij}\mathbf{R}_{ij}^H\mathbf{R}_{ij}\mathbf{F}^H + \nu_1\mathbf{F}\mathbf{F}_{u1}^H\mathbf{F}_{u1}\mathbf{F}^H \right) \mathbf{F}\mathbf{x}^{(1)}$$
$$= \mathbf{F}\sum_{ij}\mathbf{R}_{ij}^H\hat{\mathbf{x}}_{ij}^{(1)} + \nu_1\mathbf{F}\mathbf{F}_{u1}^H\mathbf{y}^{(1)}. \quad (12)$$

The matrix $\mathbf{F}\mathbf{F}_{u1}^H\mathbf{F}_{u1}\mathbf{F}^H$ is a diagonal matrix consisting of ones (corresponding to sampling locations in k-space) and zeros. Under the "wrap around" assumption, $\mathbf{F}\sum_{ij}\mathbf{R}_{ij}^H\mathbf{R}_{ij}\mathbf{F}^H = \beta\mathbf{I}_P$. Thus, the matrix pre-multiplying $\mathbf{F}\mathbf{x}^{(1)}$ in (12) is diagonal and trivially invertible. The vector $\mathbf{F}\mathbf{F}_{u1}^H\mathbf{y}^{(1)}$ represents the zero-filled Fourier measurements. Dividing both sides of (12) by the constant β to obtain

$$\tilde{\mathbf{y}}_{pq}^{(1)} = \begin{cases} \left(\mathbf{F}\hat{\mathbf{x}}^{(1)} \right)_{pq}, & (p,q) \notin \Omega^{(1)} \\ \frac{1}{1+\tilde{\nu}_1} \left(\mathbf{F}\hat{\mathbf{x}}^{(1)} + \tilde{\nu}_1\mathbf{F}\mathbf{F}_{u1}^H\mathbf{y}^{(1)} \right)_{pq}, & (p,q) \in \Omega^{(1)} \end{cases}$$

where $\tilde{\nu}_1 = \nu_1/\beta$, $\hat{\mathbf{x}}^{(1)} = \frac{1}{\beta}\sum_{ij}\mathbf{R}_{ij}^H\hat{\mathbf{x}}_{ij}^{(1)}$ denotes the denoised image. We denote by $\Omega^{(1)}$ the subset of k-space that has been sampled and by $\tilde{\mathbf{y}}_{pq}^{(1)}$ the updated value at location (p,q) in the k-space. Note that (8) uses the dictionaries that were learned in Stage 1) to interpolate the non-sampled Fourier frequencies, and update the sampled frequencies. Then, we immediately obtain the solution:

$$\tilde{\mathbf{x}}^{(1)} = \mathbf{F}^H\tilde{\mathbf{y}}^{(1)} \quad (13)$$

where $\mathbf{F}^H$ denotes the conjugate Fourier transform matrix. $\tilde{\mathbf{y}}^{(1)}$ denotes the estimated k-space samples as in (8). In other words, the estimation $\tilde{\mathbf{x}}^{(1)}$ is obtained by inverse DFT of $\tilde{\mathbf{y}}^{(1)}$. Then the process returns to the Stage 1). The whole process is shown in Algorithm 1.

---

[1]Note that $\mathbf{z}^k$ is a row vector resulting from the derivative w.r.t the k-th atom pair, while $\mathbf{z}_{ij}$ is a column vector corresponding to the ij-th patch pair.

[2]In particular, $\beta = n$ when the overlap stride $r = 1$, where the *overlap stride* is defined as the distance in pixels between corresponding pixel locations in adjacent image patches.

Appendix B: More Experiments

Tissue can be characterized by two different relaxation times – T1 (longitudinal relaxation time) and T2 (transverse relaxation time).[3] T1-weighted and T2-weighted pair of MRI scans are two basic types of multi-contrast data, where the former is produced by using short TE and TR times and conversely the latter is produced by using longer TE (Time to Echo) and TR (Repetition Time) times. In general, T1-weighted MRI images results in highlighted/bright fat tissue, such as subcutaneous fat (SC fat) and bone marrow, and suppressed/dark water-based tissue, such as Cerebrospinal fluid (CSF). In contrast, T2-weighted MRI images highlight both fat tissue and water-based tissue. Therefore, the correlation of T1-weighted and T2-weighted is complex, instead of simple reverse mapping relationship.

In this experiment, we use under-sampled T1-weighted MRI as the target contrast and corresponding fully-sampled T2-weighted as the guidance contrast to replicate the same scenario as in [3]. Similar to previous approaches [3, 9, 12, 28–30], the data acquisition was simulated by retrospectively under-sampling the 2D discrete Fourier transform of clinical magnitude MR images.[4] The sampling masks include Cartesian 1D and 2D random sampling. We compare the proposed approach with DLMRI [9] to show the benefits of integrating guidance information into the MRI reconstruction task. We also compare with SVTMRI [3] which uses the structure-guided total variation to integrate the guidance contrast to aid the reconstruction of the target one.Figure 3 and 4 show reconstruction results for the scenario where a variable density Cartesian mask is employed for under-sampling on the target T1-weighted contrast, with a fully sampled T2-weighted MRI for guidance contrast.

---

[3]T1 (longitudinal relaxation time) is a measure of the time taken for excited spinning protons to realign with the external magnetic field and return to equilibrium. T2 (transverse relaxation time) is a measure of the time taken for excited spinning protons to lose phase coherence among the nuclei spinning perpendicular to the main field.

[4]After using the Fourier transform to transform measured k-space data into image space, the image data is of complex type, which is then manipulated for different clinical utility. In clinical practice, magnitude images are nearly exclusively used for diagnosis as it maximizes the signal-to-noise ratio (SNR). Phase-images are occasionally generated in clinical MRI for the depiction of flow and characterization of susceptibility-induced distortions. Therefore, from the perspective of diagnosis, we focus on the magnitude images
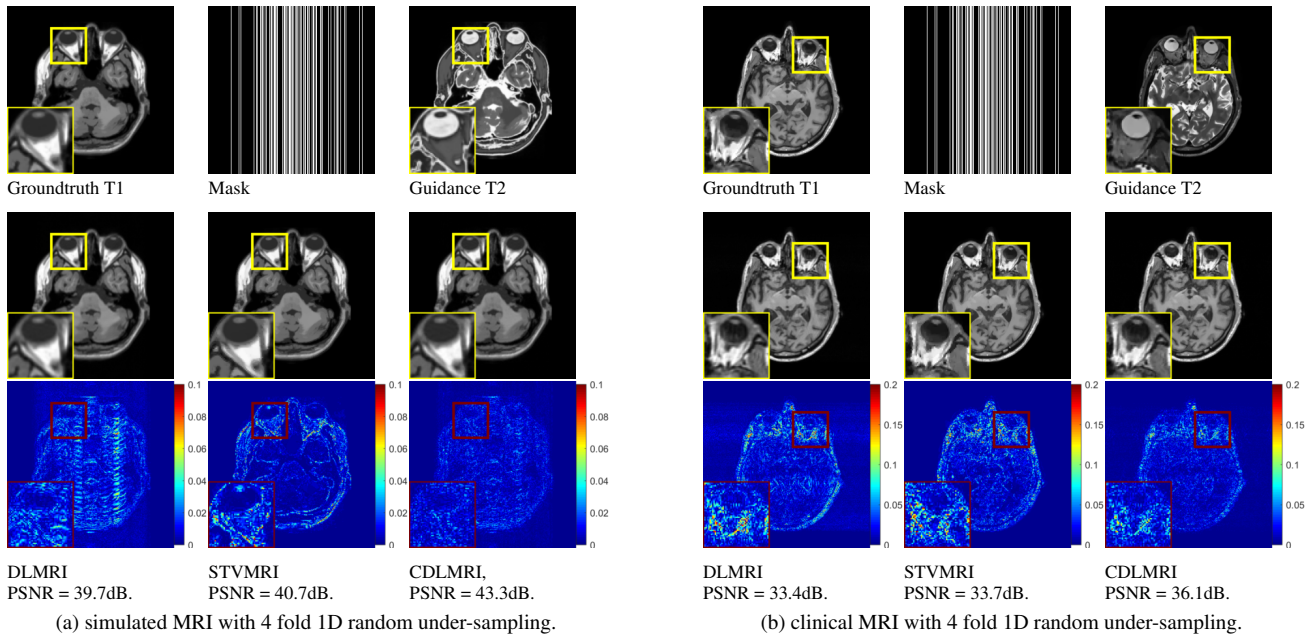
Groundtruth T1 | Mask | Guidance T2
Groundtruth T1 | Mask | Guidance T2

DLMRI
PSNR = 39.7dB.
STVMRI
PSNR = 40.7dB.
CDLMRI,
PSNR = 43.3dB.

DLMRI
PSNR = 33.4dB.
STVMRI
PSNR = 33.7dB.
CDLMRI
PSNR = 36.1dB.

(a) simulated MRI with 4 fold 1D random under-sampling.

(b) clinical MRI with 4 fold 1D random under-sampling.

Fig. 3. Reconstruction for T1-weighted MRI, with fully-sampled T2-weighted version as reference using 4 fold Cartesian 1D random under-sampling. The first row shows the groundtruth T1-weighted contrast, sampling mask and guidance T2-weighted contrast. The second and third rows show the reconstructed images and the corresponding residual error from DLMRI [9], STVMRI [3], and the proposed CDLMRI. It can be seen that the proposed approach reliably reconstructs fine details and substantially suppresses aliasing, noise and artifacts, leading to the smallest residual error.
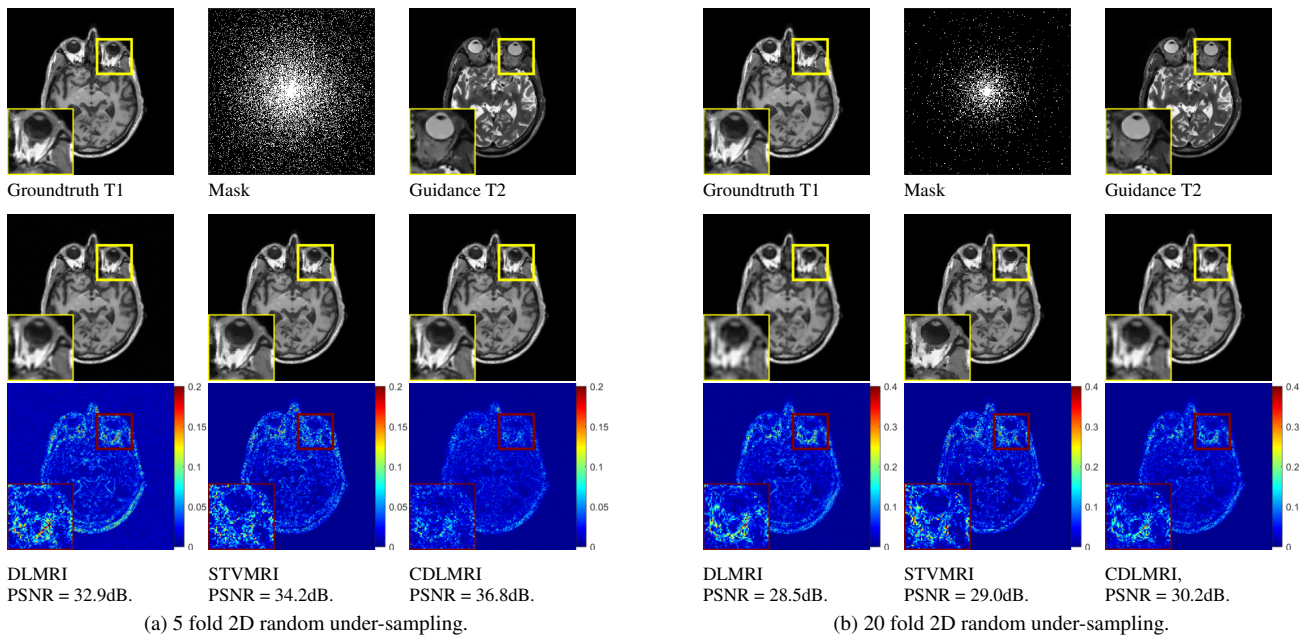

Groundtruth T1 | Mask | Guidance T2
Groundtruth T1 | Mask | Guidance T2

DLMRI
PSNR = 32.9dB.
STVMRI
PSNR = 34.2dB.
CDLMRI
PSNR = 36.8dB.

DLMRI
PSNR = 28.5dB.
STVMRI
PSNR = 29.0dB.
CDLMRI,
PSNR = 30.2dB.

(a) 5 fold 2D random under-sampling.

(b) 20 fold 2D random under-sampling.

Fig. 4. Reconstruction for T1-weighted MRI, with fully-sampled T2-weighted version as reference using 5 fold and 20 fold 2D random under-sampling, using DLMRI [9], STVMRI [3], and the proposed CDLMRI. The first row shows the groundtruth T1-weighted, sampling mask and guidance modality T2-weighted. The second and third rows show the reconstructed images and the corresponding residual error from DLMRI [9], STVMRI [3], and the proposed CDLMRI. It can be seen that the proposed approach outperform the competing approaches, leading to the smallest residual error.